

Screen-Printed Soft Capacitive Sensors for Spatial Mapping of Both Positive and Negative Pressures

Hongyang Shi, Mohammed Al-Rubaiai, Christopher M. Holbrook, Jinshui Miao, Thassy Pinto, Chuan Wang,* and Xiaobo Tan*

Soft pressure sensors are one class of the essential devices for robotics and wearable device applications. Despite the tremendous progress, sensors that can reliably detect both positive and negative pressures have not yet been demonstrated. In this paper, a soft capacitive pressure sensor, made using a convenient and low-cost screen-printing process that can reliably detect both positive and negative pressures from -60 to 20 kPa, is reported. The sensor is made with an Ecoflex-0030 dielectric layer, conductive and stretchable poly(3,4-ethylenedioxythiophene):poly(styrenesulfonate) (with ionic additives) electrodes, and polydimethylsiloxane encapsulation layers. Air gaps are designed and incorporated into the dielectric layer to significantly enhance the sample deformation and pressure response especially to negative pressure. The sensor exhibits repeatable response for thousands of cycles, even under bending or stretching conditions. Lastly, to demonstrate the practical application, a 12×12 -pixel sensor array that can automatically measure both positive and negative pressure distributions has been reported under -20 and 10 kPa.

Many of these applications require positive pressure sensing^[3–6] while others demand the capability of measuring negative pressure. Examples include the detection of suction events from lamprey's mouth^[7] or octopus' suction cups^[8] and measuring surface pressure distribution of cars during on-road driving.^[9] Soft pressure sensors can be formed based on various transducing principles, such as piezoresistive sensing,^[3,10–17] piezoelectric sensing,^[18] capacitive sensing,^[19–28] and transistor mechanism.^[25,29] Piezoresistive pressure sensors generally exhibit good sensitivity under compressive loads but the noise present in the resistivity measurements can be significant due to their relatively high resistivity,^[19] and the layers of piezoresistive sensors tend to delaminate under negative pressure, which cuts off the current flow in the piezoresistive materials. Piezoelectric pressure sensing

1. Introduction

Soft pressure sensors are promising for various applications including wearable electronic skins,^[1–4] soft robotics,^[5] environmental monitoring,^[6–8] and aerodynamic control of vehicles.^[8]

foil^[18] shows hysteresis in response because of the characteristics of piezoelectric materials and the crosstalk in the sensor matrix is often great. Moreover, to our best knowledge, no work has been reported so far on using piezoelectric sensors for negative pressure detection. Flexible pressure-sensitive organic thin film transistors^[25,29] rely on the gate dielectric layer to convert the pressure input to change in the drain current, despite the high sensitivity, the multiple layers in the sensor films could delaminate under negative pressure and thus cause sensor failure. Capacitive pressure sensors can also be made using simple parallel-plate capacitor^[30] or crossbar capacitor structures,^[31] where the capacitance is proportional to the area and inversely proportional to the spacing between the two parallel electrodes. Ideally, such structures should be able to detect both positive and negative pressure because the spacing between the electrodes will decrease when the sensor is compressed (positive pressure) and increase when under partial vacuum (negative pressure). Nevertheless, soft capacitive pressure sensors are actually insensitive to negative pressure because of the visco-elasticity of the materials in the substrate, resulting in very small thickness change of the dielectric layer under negative pressure.

In order to improve the sensitivity of soft pressure sensors, a number of strategies have been proposed including fabricating microstructures in the conducting materials or dielectric layers. Bao's research group firstly introduced micro pyramid features

H. Shi, M. Al-Rubaiai, T. Pinto, Prof. X. Tan
Electrical & Computer Engineering
Michigan State University
East Lansing, MI 48824, USA
E-mail: xbtan@egr.msu.edu

Dr. C. M. Holbrook
Hammond Bay Biological Station
United States Geological Survey
Millersburg, MI 49759, USA

Dr. J. Miao
Electrical and Systems Engineering
University of Pennsylvania
Philadelphia, PA 19104, USA

Prof. C. Wang
Electrical and Systems Engineering
Washington University in St. Louis
St. Louis, MO 63130, USA
E-mail: chuanwang@wustl.edu

 The ORCID identification number(s) for the author(s) of this article can be found under <https://doi.org/10.1002/adfm.201809116>.

DOI: 10.1002/adfm.201809116

into the dielectric layers of pressure sensors, gaining good sensitivity and short response time.^[4,25,29] Hasan et al.^[11] designed micro pillars in their pressure sensors to enhance the sensitivity under gentle touch, and the micropillar-based pressure sensors were also reported in Park et al.^[15] and Engel et al. work.^[19] In addition, guided mechanical cracks,^[16,32] hierarchical structure,^[33] interlocked microdome structures,^[34,35] and porous insulation layer^[13,14,22,28] have all been demonstrated to improve the performance of pressure sensors. All these microstructures would increase the number of conducting paths and conducting area in the materials, or augment the dielectric performance when the sensor films are compressed, which drastically enhances the conductivity and sensitivity of the pressure sensors. Nevertheless, most of these sensor designs would fail to work under negative pressure because the current flow would be cut off when the multilayers delaminate under negative pressures. Under negative pressure, the sensor needs to not only be responsive to negative pressure, but also form a good bonding between the layers in order to endure negative pressure and avoid delamination. A diaphragm structure that is well bonded with its substrate can easily deform under both negative and positive pressures, and the corresponding deformation can be converted to change in capacitance when the structure is constructed as a capacitor. Taking the above into consideration, a capacitive pressure sensor with a diaphragm structure^[20,23,26] that deflects by external pressure has become a promising solution for measurement of both positive and negative pressures. The thin diaphragm instead of the entire sample deflects under external pressure, which enlarges the spacing change between the two electrodes and could be measured from the capacitance change. Lee et al.^[23] fabricated a modular expandable tactile sensor in the diaphragm structure using polydimethylsiloxane (PDMS) substrate and copper strip electrodes, and Nie et al.^[26] reported a similar transparent iontronic film for capacitive pressure sensing using polyethylene terephthalate (PET) films. However, these sensors are not stretchable due to the copper electrodes and PET films used, and the responses to negative pressure have not been reported yet. To achieve soft pressure sensors that are stretchable, conductive nanomaterials such as graphene,^[16,17] carbon nanotubes,^[10,24] metal nanowires,^[3,27,36] conducting oxides,^[11,20,22,25,26,28,29] or conducting polymers^[14,37,38] could be used.

Based on our preliminary work,^[39] in this paper, we present a convenient and low-cost process for fabricating a soft capacitive sensor that is stretchable and responsive to both positive and negative pressures. The sensor is comprised of a soft Ecoflex-0030 dielectric layer sandwiched in between and tightly bonded with screen-printed poly(3,4-ethylenedioxythiophene):poly(styrenesulfonate) (PEDOT:PSS) electrodes and PDMS encapsulation layers. More importantly, air gap channels are incorporated and uniformly distributed in the Ecoflex-0030 layer, which shape the diaphragm structures that greatly enhance the dielectric layer deformation under an external pressure, resulting in significantly improved response, especially to negative pressure. Meanwhile, the PEDOT:PSS electrodes are encapsulated on the Ecoflex-030 substrate with PDMS layers, which successfully protect the electrodes and prevent the layers from delamination under negative pressure. The response of the single pixel sensor is systematically characterized and finite element

method (FEM) simulation is used to study the influence of the air gap geometry on the sensor response. The sensor with optimized design exhibits good sensitivity from -60 to 20 kPa and great repeatability under compressive loads, vacuum suction, and even bending or stretching conditions. Lastly, a 12×12 -pixel sensor array that can automatically measure the pressure distribution for both positive and negative pressures with high fidelity is demonstrated. With its performance, versatility, and facile fabrication, the soft pressure sensor demonstrated in this paper may find a wide practical applications in soft robotics and wearable electronics.

2. Results and Discussion

2.1. Fabrication of the Soft Capacitive Pressure Sensors with Air Gap Channels

A crossbar array of soft capacitive pressure sensors is designed and fabricated and its schematic is illustrated in **Figure 1a**. The soft capacitive pressure sensor is comprised of an Ecoflex-0030 dielectric layer sandwiched in between conductive polymer PEDOT:PSS electrodes and PDMS encapsulation layers. The Ecoflex-0030 dielectric layer is 1.4 mm thick with multiple air gap channels (height: 0.5 mm, width: 1.2 mm, spacing: 1.5 mm) uniformly distributed in the center. As will be discussed later, these air gap channels play a critical role in the sensing of both positive and negative pressure by significantly enhancing the deformation of the dielectric layer under pressure, thereby increasing the sensitivity. PEDOT:PSS polymer is used as the electrode due to its high conductivity (sheet resistance of $\approx 34 \Omega$ per sq) and ionic additive bis(trifluoromethane)sulfonimide lithium salt is incorporated into the PEDOT:PSS to further improve its stretchability.^[38] **Figure 1b** shows the bright field optical images and scanning electron microscopy (SEM) image of the cured PEDOT:PSS film with ionic additive transferred on a Si wafer with very good uniformity.

The picture of a completed 12×12 soft capacitive pressure sensor array is shown in **Figure 1c** and its fabrication process is illustrated in **Figure 1d**. First, an Ecoflex-0030 dielectric layer is cast in a mold on a treated glass plate with uniformly distributed 0.5 mm thick and 1.2 mm wide polycarbonate strips. After the Ecoflex-0030 is cured, the polycarbonate strips are removed, resulting in the Ecoflex-0030 film with built-in air gap channels. A 0.5 mm thick PEDOT:PSS film is then screen-printed onto one side of the Ecoflex-0030 dielectric layer with the PEDOT:PSS electrodes patterned in parallel but perpendicular to the air gap channels. After curing by heating up at 70 °C for 1 h, the PEDOT:PSS electrodes were encapsulated by a 0.7 mm thick PDMS layer (PDMS base:curing agent = $10:1$ wt%). This encapsulation layer effectively protects the PEDOT:PSS electrodes from cracking under external force and also forms a very strong bonding between PDMS and Ecoflex-0030 substrate, preventing the sandwiched layers from delamination when negative pressure is applied. Next, the device is peeled off from the glass plate and placed upside down. The PEDOT:PSS screen-printing and PDMS encapsulation process are then repeated on the other side of the Ecoflex-0030 dielectric with the newly patterned PEDOT:PSS electrodes orthogonal

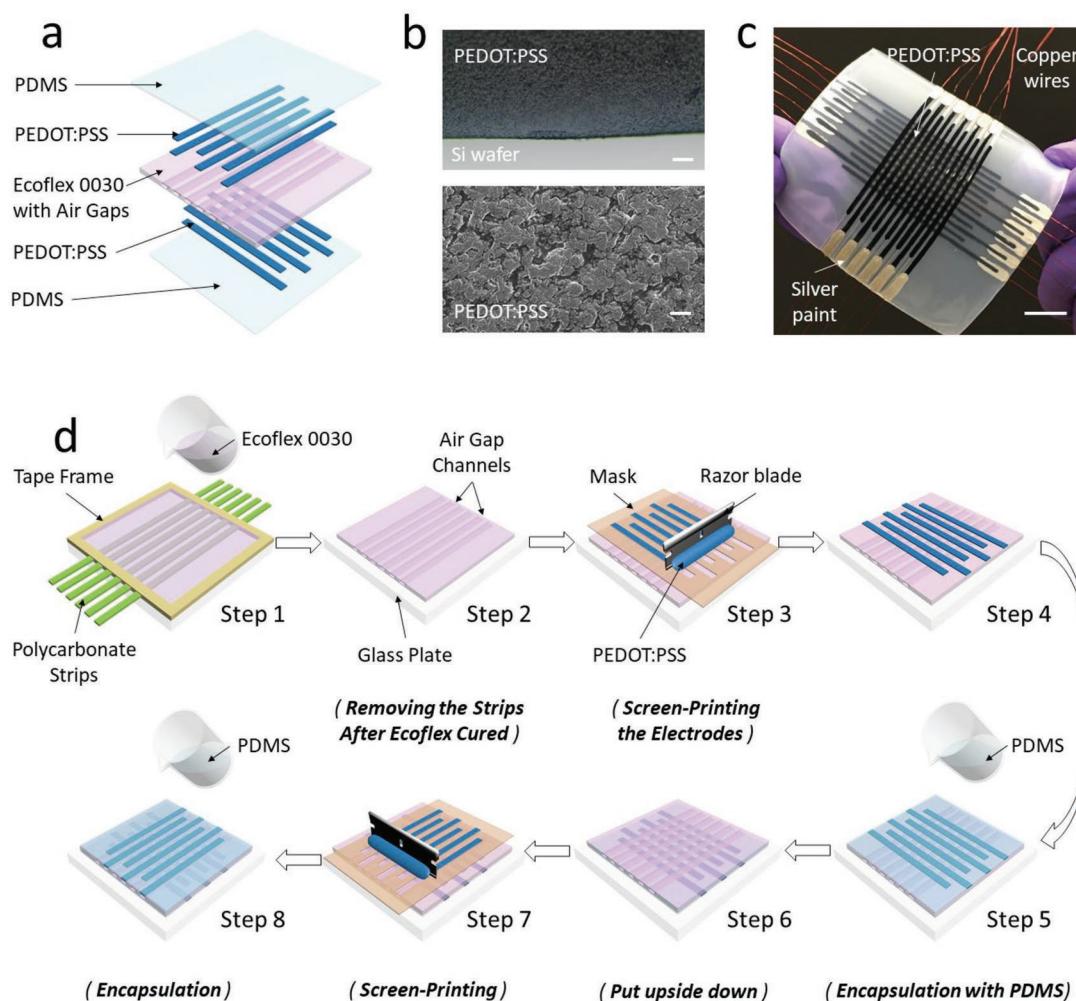


Figure 1. a) Schematic illustration of the soft capacitive pressure sensor array with air gap channels and conductive polymer PEDOT:PSS electrodes. b) Optical micrograph (top) and SEM image (bottom) of the screen-printed PEDOT:PSS film with a feature thickness of ≈ 200 μm . The PEDOT:PSS contains 10:1 wt% bis(trifluoromethane)sulfonimide lithium salt as stretchability and electrical conductivity enhancer. Scale bars: 20 and 2 μm , respectively. c) Photograph of a 12 \times 12 capacitive pressure sensor array. Scale bar: 1 cm. d) Schematic illustrating the fabrication procedures of the soft capacitive pressure sensor array.

to the previous electrodes in order to form a crossbar capacitor array. Also, this layer of patterned PEDOT:PSS electrodes should be aligned with the air gap channels in the substrate so that the electrodes could conform with the deformation of the diaphragms in case of cracking.

2.2. Characterization of the Single-Pixel Sensors

The effect of the air gap channel geometry on the performance of the single-pixel sensors is investigated. The devices are characterized by measuring the relative change in capacitance as a function of pressure ($\Delta C/C_0$ vs P) and the results are shown in **Figure 2**. Figure 2a presents the structure of the single-pixel sensor with height (H), width (W), and the number (N) of the air gap channels labeled in the figure. Six groups of air gap parameters have been selected, three devices have been fabricated for each configuration (see Figure S1 in the Supporting Information for sample sensors) and three rounds of measurements

have been taken for each device to obtain the average response performance (see Figure S2 for experimental setups in the Supporting Information). The error bar in Figure 2a represents the standard error of the mean for each group of testing points. As shown in Figure 2b and Figure S3 (Supporting Information), all five configurations respond similarly to positive pressure and exhibit a monotonic increase in relative change in capacitance with increasing pressure. The pressure response also increases with increasing air gap size, reaching a maximum $\Delta C/C_0$ value of 4.01%, 6.15%, 7.16%, 8.10%, 9.48% at a positive pressure of 20 kPa, for the sensors without air gap, and with air gap of dimensions $H = 0.3$ mm and $W = 1.2$ mm, $H = 0.5$ mm and $W = 1.2$ mm, $H = 0.5$ mm and $W = 1.6$ mm, and $H = 0.5$ mm and $W = 2.0$ mm, respectively.

For sensing a negative pressure, the importance of having an air gap channel in the dielectric layer becomes evident as the sensor without an air gap channel fails to respond properly and exhibits negligible capacitance change as the pressure changes between 0 and -30 kPa. The slight increase of $\Delta C/C_0$

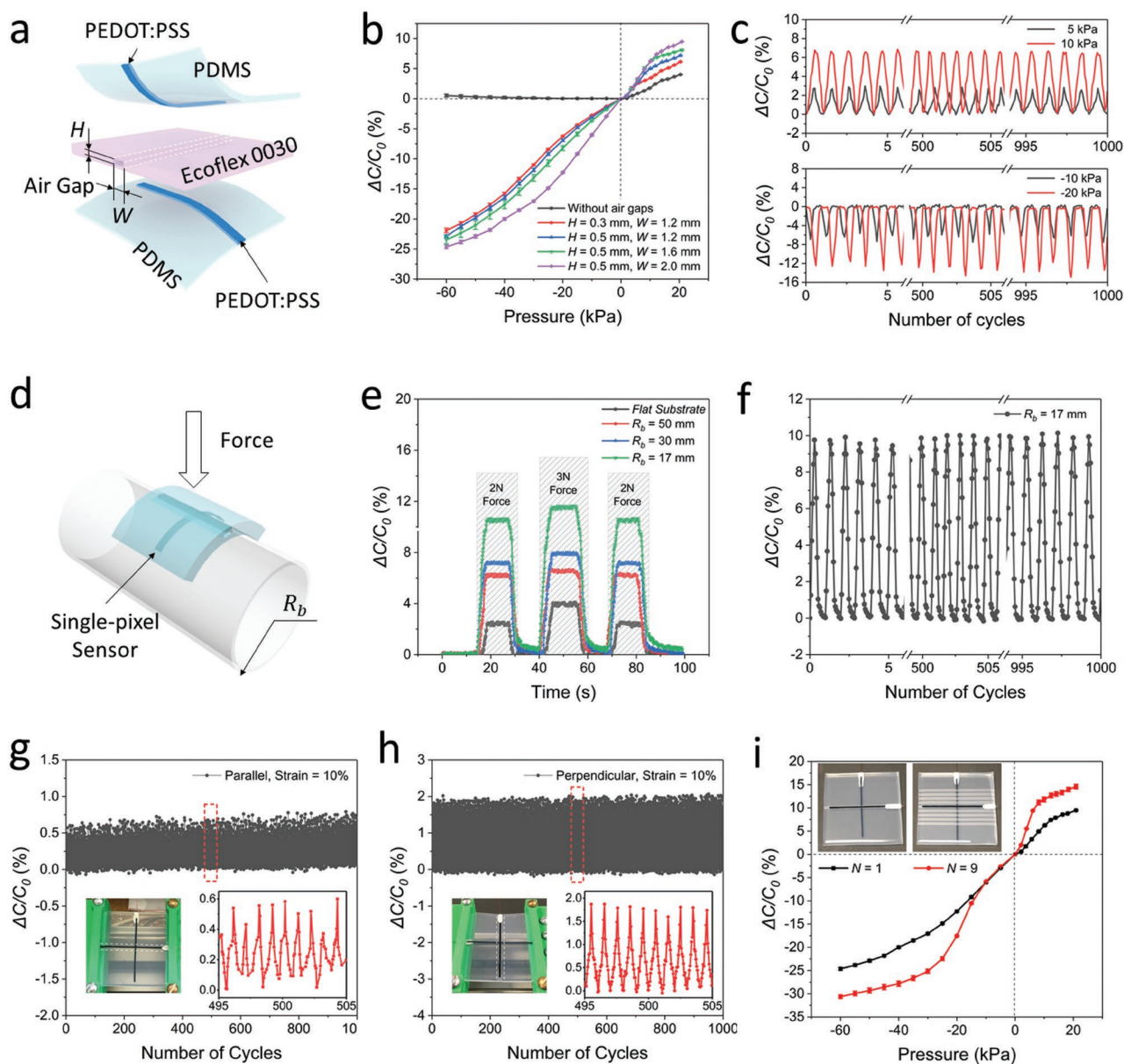


Figure 2. Characterization of a single-pixel soft capacitive pressure sensor. a) Schematic diagram representing the multilayer structure of the single capacitive pressure sensor. b) Relative change in capacitance in response to applied pressure for a single-pixel capacitive pressure sensor with various configurations of air gap in the Ecoflex dielectric layer. c) Cyclic test of the sensor response for 1000 cycles at different pressures. d) Schematic illustration of the sensor in the bent state under normal force. e) Pressure response of the sensor with air gap ($H = 0.5$ mm, $W = 2.0$ mm) under a sequence of normal forces, 2, 3, and 2 N when the sensor is bent to curvature radii of 50, 30, and 17 mm, respectively. f) Cyclic test of the sensor at a bending radius of 17 mm for 1000 cycles. g) Cyclic stretching test of the sensor with air gap ($H = 0.5$ mm, $W = 2.0$ mm) at 10% strain with the air gap direction parallel to the stretch direction. h) Cyclic stretching test of the sensor with air gap ($H = 0.5$ mm, $W = 2.0$ mm) at 10% strain with the air gap direction perpendicular to the stretch direction. i) Static pressure responses of a single-pixel sensor with one air gap ($H = 0.5$ mm, $W = 2.0$ mm) and a single-pixel sensor with nine air gaps ($H = 0.5$ mm, $W = 2.0$ mm).

between -30 and -60 kPa can be attributed to the interior of the suction cup pressing against the surface of the sensor under vacuum. In contrast, for the sensors with air gap channels, $\Delta C/C_0$ decreases monotonically as the pressure varies from 0 to -60 kPa, reaching -21.91% , -22.90% , -23.46% , and -24.64% for the sensor with air gap $H = 0.3$ mm and $W = 1.2$ mm, $H = 0.5$ mm and $W = 1.2$ mm, $H = 0.5$ mm and $W = 1.6$ mm, and $H = 0.5$ mm and $W = 2.0$ mm, respectively. Here, the

sensor with air gap $H = 0.5$ mm and $W = 2.0$ mm achieves the best sensing performance among all the air gap configurations. **Table 1** summarizes the calculated sensitivity (defined as the slope of the relative change in capacitance to pressure response curve, $S = d(\Delta C/C_0) / dP$) of the five types of sensors above for different pressure ranges. Basically, a larger air gap would result in sensors with higher sensitive to both negative and positive pressure.

Table 1. Sensitivity of the single-pixel sensors with different air gap configurations.

Sensitivity [%/kPa]	−60 to −20 [kPa]	−20 to 0 [kPa]	0 to 10 [kPa]	10 to 20 [kPa]
Without air gap	–	–	0.18	0.13
$H = 0.3$ mm, $W = 1.2$ mm	0.34	0.30	0.38	0.15
$H = 0.5$ mm, $W = 1.2$ mm	0.34	0.34	0.56	0.13
$H = 0.5$ mm, $W = 1.6$ mm	0.35	0.40	0.62	0.12
$H = 0.5$ mm, $W = 2.0$ mm	0.30	0.56	0.77	0.15

The repeatability of the device is also evaluated on the sensor with air gap $H = 0.5$ mm and $W = 2.0$ mm by cyclic test with 1000 repetitions for four pressure levels: 5, 10, −10, and −20 kPa. As illustrated in Figure 2c, the device can preserve stable response throughout the 1000 cycles for all pressure levels (Figure S4, Supporting Information).

In order to demonstrate the capability of the soft capacitive pressure sensor working on curved surfaces, we examine the device's response to pressure when attached onto a pipe, as illustrated in Figure 2d (Figure S5, Supporting Information). Figure 2e presents the response of the sensor with air gap $H = 0.5$ mm and $W = 2.0$ mm to pressure when mounted on cylindrical surfaces with various radii ($R_b = 50, 30,$ and 17 mm; Figures S5 and S6, Supporting Information). Again, three rounds of measurements are taken on each cylindrical surface when the sensor sample is tested under a sequence of force 2, 3, and 2 N for about 20 s at each stage (Figure S7, Supporting Information). The response curves reveal that the sensor is more sensitive to compressive load when it is bent on a curved substrate compared to a noncurved substrate. Furthermore, the smaller the bending radius is, the higher the relative change in capacitance would be. This is because when the sensor is in a bent state, the compressive load will have a smaller contact surface area with the sensor device, thereby the effective pressure applied on the electrodes and air gap channel would be much higher and the corresponding larger deformation will cause more change in capacitance. The sensor also exhibits good repeatability in pressure response even when bent with a radius of 17 mm as shown in Figure 2f (Figure S8, Supporting Information).

The stretchability of the single-pixel sensor is tested (Figure S9 (Supporting Information) shows the stretching experiment setup). Tensile strain is applied along two directions, parallel, and perpendicular to the air gap channel. As illustrated in Figure 2g, when the strain is set to 10% with a loading-unloading period of 12 s, the response ($\Delta C/C_0$) would increase by about 0.5% every time when stretching. For the stretching direction perpendicular to the air gap channel as shown in the inset in Figure 2h, in each period the response would increase and decrease by about 1.8%. This change in capacitance is reasonable according to the Poisson effect, which is that a material tends to compress in directions perpendicular to the direction of expansion. And for the case in Figure 2h, since the air gap is perpendicular to the stretching direction, the sensor substrate would more easily deform. On the other hand, for both stretching directions, the overall response would increase slightly by about 0.1% after 1000 cycles. This increase of about 0.1% might be attributed to be the results of

the sliding of the sensor substrate from the clamps in the experiment setup. We also try to increase the strain to 11% and test for 450 cycles during the experiment (Figure S10, Supporting Information). The increased strain leads to a crack in PEDOT:PSS electrode at the intersection point between PEDOT:PSS and the silver paint, which is used for connecting and fixing the copper wire to the PEDOT:PSS electrode. For better stretchability, the silver paint can be replaced with some other stretchable conductive glue or liquid metal.

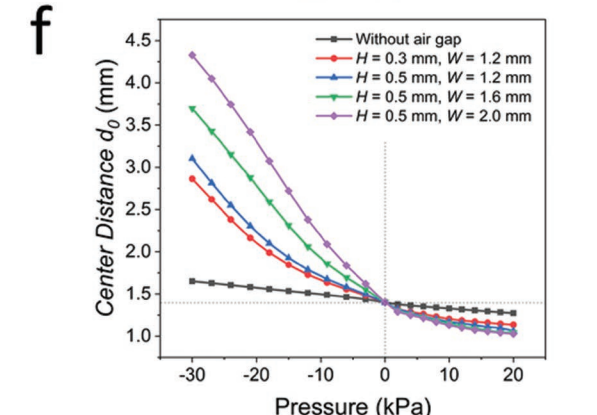
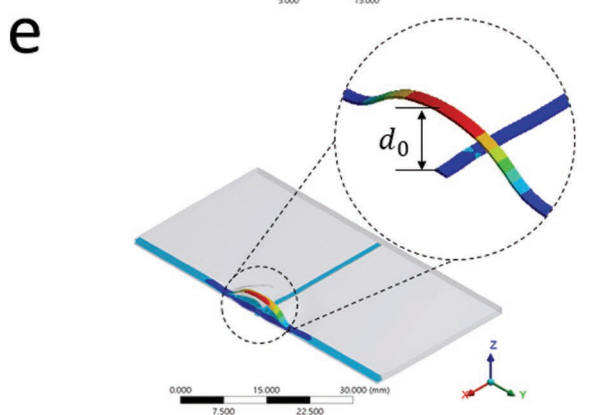
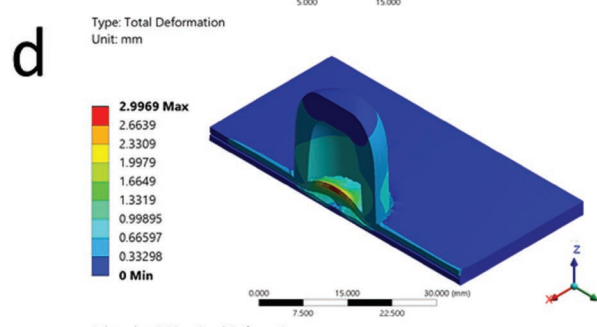
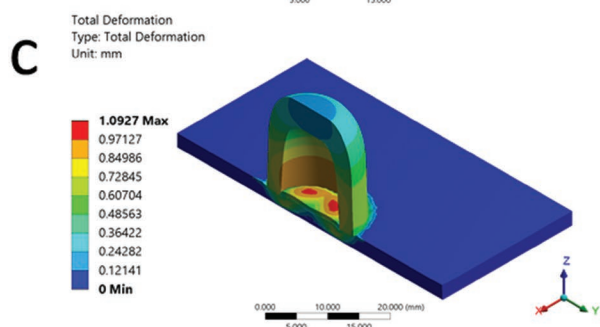
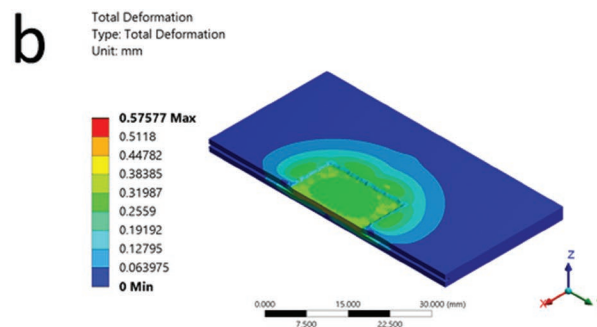
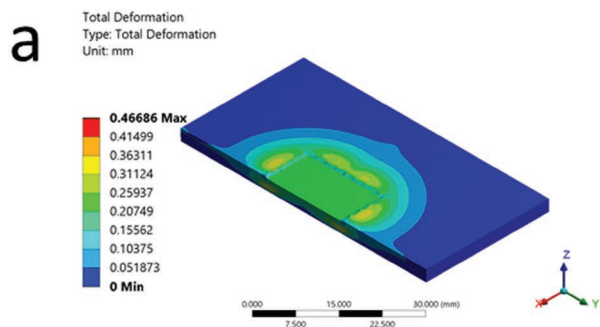
It is worth noting that this section focuses on the characterization of the single pixel sensor with a single air gap channel in the Ecoflex-0030 dielectric layer located right underneath the electrode. For the single pixel sensor where there are multiple air gap channels distributed evenly in the dielectric layer, the sensitivity of this single pixel sensor under both positive and negative pressure would be much higher. As demonstrated in Figure 2i, the single pixel sensor with nine air gap channels ($H = 0.5$ mm, $W = 2.0$ mm) can achieve relative change in capacitance of about 15% at 20 kPa and −32% at −60 kPa, which are more sensitive than the sensor with only one air gap channel as characterized in Figure 2b. This is also true for the sensor array with multiple air gap channels, which has higher sensitivity to both positive and negative pressures than a single pixel sensor with only one air gap channel, as will be explained in Section 2.4.

2.3. Finite Element Simulation

As discussed in Section 2.2, the geometry of the air gap channel has significant influence on the sensitivity of the sensor responses. Therefore, studying the mechanical properties of Ecoflex-0030 rubber, PDMS silicone, and PEDOT:PSS conductive polymers is essential for understanding the pressure-induced deformation of the sensor and the capacitive response under external pressures. In this section, we use these material properties to set up the finite element analysis models of the soft capacitive pressure sensor under both positive and negative pressures and examine the distance change in between the two electrodes as well as the vertical deformation of the whole sensor.

The finite element analysis modeling is conducted in ANSYS Workbench and one static structural module is used to build up four separate analysis models: a sensor without air gap channel under +20 and −30 kPa pressure and a sensor with air gap channel under +20 and −30 kPa pressure. The positive pressure is applied onto a glass slide (20 mm × 18 mm × 1 mm) which is placed on the sensor (60 mm × 60 mm × 2.8 mm) in the center, while the negative pressure is applied on the surface of the sensor in the region beneath the suction cup ($\phi 20.5$ mm × $\phi 14.5$ mm × 15 mm in depth) with Dragon Skin 30 as the assigned material, and the air gap channel in the dielectric layer designed with dimensions $H = 0.5$ mm and $W = 2.0$ mm.

Four materials of interest are the silicone materials (Ecoflex-0030, PDMS 10:1, Dragon Skin 30), and conductive



polymer PEDOT:PSS. To characterize the material properties of the silicones, a uniaxial tensile test is performed following the D412-15a standard.^[40] The dumbbell test samples are stretched at a speed of 500 mm min⁻¹. Five samples of each material are stretched using a tensile tester (Universal Testing Machine 3345, Instron, see Figure S11 in the Supporting Information) and the average stress strain data obtained from the five samples are used in the finite element analysis by data fitting to obtain the best fitted hyperelastic models. The Mooney-Rivlin 3 parameter model^[41,42] proves to be the best constitutive model for Ecoflex-0030 with parameters $C_{10} = 90.523$ Pa, $C_{01} = 10\,137$ Pa, and $C_{11} = 0.0504$ Pa; the Yeoh 3rd order model^[43] proves to be the best model for PDMS with parameters $C_{10} = 2474.5$ Pa, $C_{20} = 0.00297$ Pa, and $C_{30} = 1.498E-7$ Pa; and the Ogden 1st order model^[44] turns out to be the best one for Dragon Skin 30 with parameters $\alpha_1 = 2.717$, $\mu_1 = 0.158$ MPa (Equations (1)–(3), Supporting Information). For PEDOT:PSS (thickness range 150–200 μm) with 10 wt% of bis(trifluoromethane)-sulfonimide lithium salt, an isotropic elastic model with Young's modulus 55 MPa is used according to the report.^[38]

Under a positive pressure, the sensor is compressed and the air gap channel in the dielectric layer will be squeezed. Note that the top and bottom surface of the air gap channel cannot penetrate each other in reality, hence in the simulation, we define a frictional contact between these two surfaces with a friction coefficient of 1.5, and this constraint condition will work once these surfaces contact each other. When a negative pressure is applied, the top surface of the sensor beneath the suction cup is pulled up, and the air gap channel will be enlarged. **Figure 3** displays the simulation results of all four analysis models, where the top subfigures are the sectional views of the sensors under a glass slide or a suction cup, and the bottom subfigures present the Z-directional deformation of the crossbar electrodes. **Figure 3a** shows the deformation in a soft pressure sensor without an air gap under +20 kPa pressure, in which the distance between the top and bottom electrodes decreases by -0.20 mm. In contrast, as shown in **Figure 3b**, the total deformation in a sensor with an air gap results in the electrode spacing decreasing by -0.51 mm. Similarly, the data in **Figure 3c,d** show that under a negative pressure of -30 kPa, the sensor with an air gap channel exhibits a much larger increase in electrode spacing (2.87 mm) compared to the sensor without an air gap channel (0.59 mm). In both cases, the larger deformation in the device with an air gap will result in larger capacitance change and better sensitivity to pressure. These four simulation results further validate the necessity of the air gap channel designed in the dielectric layer.

In addition, finite element models are also used to investigate the influence of dimensions (height H and width W) of the air gap channel on the deformation of the sensor device. Five configurations of the air gap channel are studied in the

simulation corresponding to the sensors' configurations in the experiments of Section 2.2. Since the deformation is not uniform along the electrodes, we focus on the center distance change between the crossbar electrodes at the center of the sensor, which is defined as d_0 as illustrated in **Figure 3e**. The distance d_0 between the crossbar electrodes is 1.4 mm initially and becomes smaller under positive pressure or larger under negative pressure. The simulation results of the central distance change for these five groups of air gap configurations are plotted in **Figure 3f**, where the sensor with larger air gap channel in width or height generates a larger change in central distance of the crossbar electrodes, and the sensor with air gap ($H = 0.5$ mm, $W = 2.0$ mm) achieves the largest change in distance under both positive and negative pressures, which is consistent with the experimental results present in **Figure 2b**. From the simulation results and according to the formula of crossbar capacitance (**Figure S12** and **Equation (4)**, Supporting Information), which is inversely proportional to the spacing between the two parallel electrodes $\frac{C}{\epsilon} \propto \frac{1}{d_0}$, we can conclude that the sensor with larger air gap channel has higher sensitivity for both positive and negative pressures, which is consistent with the experimental results in Section 2.2.

2.4. Spatial Mapping of Pressure Distributions with the Sensor Array

Based on the characterization of the single-pixel sensor with air gap channel, we extend our work to a 12×12 sensor array with air gap channels uniformly distributed underneath the top layer electrodes. A channel-selection circuit that uses NI LabVIEW program to control the communication between an Arduino Uno microcontroller board and AD7746 capacitive-to-digital converter is designed to automatically scan through all pixels with a period of 28.6 ms to measure the $\Delta C/C_0$ before and after the pressure is applied in order to determine the pressure distribution.

Taking the special mapping resolution into consideration, a 12×12 -pixel sensor array with 12 air gap channels ($H = 0.5$ mm, $W = 1.2$ mm) is fabricated (the one with $W = 2.0$ is not considered since the wider the air gap, the sparser the electrodes would be). **Figure 4a** displays the photographs of the 12×12 -pixel sensor array with air gap channels with 3D-printed M-, S-, U-, and O-shaped letter block placed on top. A loading pressure of +20 kPa is applied using a syringe pump and the pressure is set according to the contacting surface area of the letter block and the force between the loading part of the syringe pump and the letter block measured by a force sensing resistor (**Figure S13**, Supporting Information). **Figure 4b** depicts the mapping contours of relative change in capacitance with the sensor array under corresponding letter

Figure 3. FEA Simulation of the sensor with and without an air gap in the Ecoflex-0030 dielectric layer under different pressures. A–d) Sectional view of total deformation of the sensor and the corresponding Z-directional deformation between the crossbar electrodes for a) Sensor without air gap under +20 kPa pressure; b) Sensor with an air gap ($H = 0.5$ mm, $W = 2.0$ mm) under +20 kPa pressure; c) Sensor without an air gap under -30 kPa pressure applied with a suction cup; d) Sensor with air gap ($H = 0.5$ mm, $W = 2.0$ mm) under -30 kPa pressure. e) Z-directional deformation of the electrodes and the top and bottom surface of the air gap ($H = 0.5$ mm, $W = 2.0$ mm) in the sensor under -30 kPa pressure, where d_0 denotes the central distance between the crossbar electrodes. f) Distance change between top and bottom electrodes under different pressures.

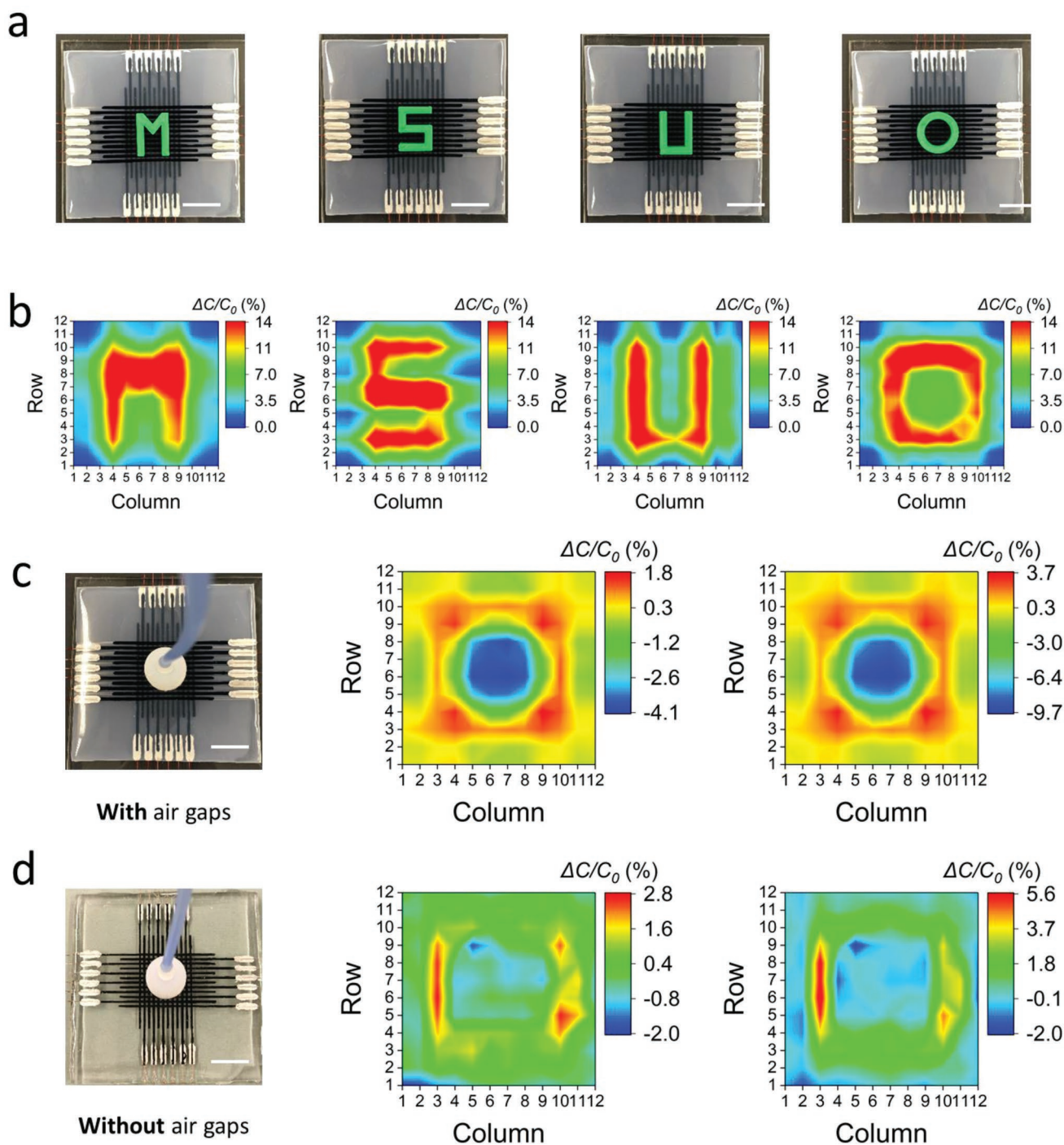


Figure 4. Spatial mapping of pressure distributions with the sensor array under both positive and negative pressures. a) Photograph of the 12×12 pixel sensor array with different shaped objects placed on top for pressure mapping testing. Scale bar: 2 cm. b) The corresponding distributions of the normalized capacitance change with +10 kPa pressure applied. c) Photograph of the 12×12 pixel sensor array with air gaps ($H = 0.5$ mm, $W = 1.2$ mm) and the corresponding contour plots of relative change in capacitance under a negative pressure of -10 kPa (left) and -20 kPa (right). Scale bar: 2 cm. d) Photograph of the 12×12 -pixel sensor array without an air gap and the corresponding contour plot of relative change in capacitance under a negative pressure of -10 kPa (left) and -20 kPa (right). Scale bar: 2 cm.

block, which are consistent with the profiles of the letter blocks used. Ideally, the relative change in capacitance could be mapped into pressure values based on the characterization of the single-pixel response. However, the single-pixel sensor

reported in Section 2.2. only has a single air gap channel in the dielectric layer, whereas the 12×12 sensor array contains 12 air gap channels uniformly distributed in the dielectric layer underneath each column. The extra air gap channels in the

sensor array increases the deformation of the sensor, which is why the sensor array exhibits $\Delta C/C_0$ of more than 14% under +20 kPa but the single-pixel sensor in Figure 2b only exhibits $\approx 7.5\%$ change at the same pressure. For the reason above, the relative change in capacitance in the mapping contour cannot be simply converted into pressure values according to the characterization in Section 2.2.

For the mapping of negative pressure, the sensor arrays with and without air gap channels ($H = 0.5$ mm, $W = 1.2$ mm, $N = 12$) exhibit drastically different results. Figure 4c presents the pressure mapping results measured by the sensor array with air gap channels under -10 and -20 kPa of pressure, where the maximum capacitance change reaches -4.1% and -9.7% , respectively. The contours also clearly show the profile of the rim of the suction cup, which is under positive pressure, and the area inside the suction cup, which is under negative pressure. In contrast, for the data collected from the sensor array without air gap (Figure 4d), the negative pressure region is indiscernible. The results highlight the significance of incorporating air gap channels in the dielectric layer of the sensor for negative pressure sensing applications.

3. Conclusion

In summary, we have reported the design of a soft capacitive sensor that is capable of measuring both positive and negative pressures. The ability to detect negative pressure, which is rarely reported in the literature, is achieved in our work by designing air gap channels in the dielectric layer between the crossbar electrodes. The air gap channels enhance the deformation of the sensor and lead to significantly improved sensitivity especially for negative pressure. The influence of the air gap geometry on the sensitivity is also systematically studied through both single-pixel measurements and finite element simulation. Based on the experimental and simulation analysis of single-pixel sensors, a 12×12 sensor array for spatial mapping of both positive and negative pressures is also demonstrated. With its convenient and low-cost fabrication process and repeatable response even when bent or stretched, our device may find a wide range of applications in soft robotics or wearable devices.

4. Experimental Section

Sensor Fabrication: A 6 in. \times 6 in. glass plate was cleaned and then treated with Rain-X water repellent, acetone, and isopropanol sequentially, followed by blow dry. Next, vinyl medium adhesion cleanroom tape was used to attach onto the glass plate to form a square-frame mold where Ecoflex-0030 would be cured. The thickness of the Ecoflex-0030 dielectric layer could be easily adjusted by changing the layers of tapes used (ten layers in this work). Polycarbonate strips (150 mm long, 1.2 mm wide, and 0.5 mm thick) with a uniform spacing of 1.5 mm were embedded in the tape frames to define the air gaps. Part A and part B of Ecoflex-0030 (Smooth-On, Inc.) were then mixed for 3 min with a 1:1 wt% mixing ratio and degassed in a vacuum chamber for 3 min at -90 kPa partial vacuum. After most of the bubbles in the Ecoflex-0030 liquid disappeared, it was poured to fill up the mold made above. After the Ecoflex-0030 film was cured at room temperature for 4 h in the mold, the tapes and polycarbonate stripes were removed, resulting in the Ecoflex-0030 dielectric layer with air gap channels.

Next, PEDOT:PSS (5.0 wt%, Sigma-Aldrich, Inc.) conductive screen printable ink with 10:1 wt% bis(trifluoromethane)sulfonimide lithium salt (Sigma-Aldrich, Inc.) were mixed for 15 min. A 0.5 mm thick polycarbonate or acrylic mask was laser-cut for screen printing and attached on the Ecoflex film with the grooves perpendicular to the air gap channels in Ecoflex. A 0.5 mm thick layer of PEDOT:PSS film was screen-printed onto the Ecoflex substrate using a razor blade with the mask. After the mask was peeled off, the PEDOT:PSS electrodes were patterned and the sample was heated to 70 °C for 1 h. After curing, the distal ends of the PEDOT:PSS electrodes were connected with a copper wire using silver paint (PELCO 16 062, Ted Pella, Inc.) as the adhesive. PDMS (Dow Sylgard 184 Silicone) with a mixing ratio of 10:1 wt% was prepared, degassed, and cast onto the Ecoflex-0030 substrate to form a 0.7 mm thick encapsulation layer on the PEDOT:PSS electrodes. After the PDMS was cured, the device was peeled off from the glass plate, placed upside down, and the PEDOT:PSS electrode patterning and PDMS encapsulation steps were repeated on the other side of the Ecoflex to form the crossbar capacitor.

Loading Positive Pressure: To apply positive pressure, a customized syringe pump (Legato 110, KD Scientific, Inc.) with 3D-printed parts (a bottom block, a loading rod, and a top block) was used. The withdraw and infuse rates and target volume were used to control the loading period and force. A 20 mm \times 18 mm \times 1 mm glass slide was placed on the sensor device in the center and the pressure was applied on top by the 3D-printed loading rod mounted on the syringe pump.

Force Measurement: To measure the actual pressure exerted by the loading rod on the soft capacitive sensor, a force sensing resistor (FSR) sensor (FSR 402, Interlink Electronics, Inc.) was placed on the loading platform. The FSR was characterized first via a voltage divider to obtain the force-voltage response curve (Figure S8, Supporting Information). Then the FSR was attached on the glass slide placed between the 3D printed loading rod and the soft capacitive sensor. The active area of the FSR sensor was $\phi 14.68$ mm, while the loading area of the loading rod was $\phi 10$ mm. When the loading rod was pressed against the soft capacitive sensor, the loading surface of the loading rod was fully covered by the FSR's active area, and the force measurement from the FSR was used to calculate the pressure applied to the sensor.

Applying Negative Pressure: A $\phi 20.5$ mm \times $\phi 14.5$ mm \times 15 mm (in depth) suction cup made of Dragon Skin 30 liquid (Smooth-On, Inc.) was fabricated by casting and molding in 3D printed polylactic acid (PLA) molds. The top outlet of the suction cup was connected to a vacuum chamber through plastic tubings and the vacuum chamber was connected to a vacuum pump, which could generate partial vacuum continuously. The vacuum chamber served as a reservoir of partial vacuum also allowed the negative pressure in the chamber to be set according to the pressure gauge on it. In the negative pressure experiments, the suction cup was placed onto the sensor device with the pump turned on.

Capacitance Measurement: AD7746 evaluation board EVAL-AD7746EB (Analog Devices, Inc.) was used to measure the capacitance, which provided a high resolution with a full-scale range of 4 pF. Given that our sensor array had 12 + 12 channels, two multiplexer breakouts (BOB-0 9056, 16-channel, SparkFun Electronics) were used in our measurement circuits. The microcontroller board Arduino Uno was used for channel selection and automatic scanning of all the sensor pixels.

Supporting Information

Supporting Information is available from the Wiley Online Library or from the author.

Acknowledgements

The authors would like to thank Dr. Peter B. Lillehoj and his student Jiran Li for sharing their laser cut machine and offering kind help for

laser cutting masks. The authors appreciate the help from Dr. Le Cai, Dr. Suoming Zhang, and Dr. Montassar Sharif on experiments and FEM simulation. The authors also acknowledge the technical services from Brian Wright and the SEM imaging guidance from Per Askeland. This work was supported in part by the Great Lakes Fishery Commission (2018-Tan-54069), the Office of Naval Research (Grant N000141512246), and an MSU Strategic Partnership Grant (16-SPG-Full-3236). Any use of trade, product, or firm names is for descriptive purposes only and does not imply endorsement by the U.S. Government.

Conflict of Interest

The authors declare no conflict of interest.

Keywords

air gap, negative pressure, PEDOT:PSS, printed electronics, soft capacitive pressure sensor

Received: December 21, 2018

Revised: March 6, 2019

Published online: April 5, 2019

- [1] M. Liu, X. Pu, C. Jiang, T. Liu, X. Huang, L. Chen, C. Du, J. Sun, W. Hu, Z. L. Wang, *Adv. Mater.* **2017**, *29*, 1703700.
- [2] L. Cai, C. Wang, *Nanoscale Res. Lett.* **2015**, *10*, 320.
- [3] S. Gong, W. Schwalb, Y. Wang, Y. Chen, Y. Tang, J. Si, B. Shirinzadeh, W. Cheng, *Nat. Commun.* **2014**, *5*, 3132.
- [4] H. H. Chou, A. Nguyen, A. Chortos, J. W. To, C. Lu, J. Mei, T. Kurosawa, W. G. Bae, J. B. Tok, Z. Bao, *Nat. Commun.* **2015**, *6*, 8011.
- [5] C. M. Boutry, M. Negre, M. Jorda, O. Vardoulis, A. Chortos, O. Khatib, Z. Bao, *Sci. Rob.* **2018**, *3*, eaau6914.
- [6] J. Park, J.-K. Kimb, D.-S. Kim, A. Shanmugasundaram, S. A. Park, S. Kang, S.-H. Kim, M. H. Jeong, D. W. Lee, *Sens. Actuators, B* **2019**, *280*, 201.
- [7] R. D. Adams, *Dissertation*, Eastern Michigan University **2006**.
- [8] W. M. Kier, A. M. Smith, *Integr. Comp. Biol.* **2002**, *42*, 1146.
- [9] A. Kremheller, *SAE Tech. Pap.* **2014**, *1*, 572.
- [10] A. Bsoul, M. S. M. Ali, K. Takahata, *Electron. Lett.* **2011**, *47*, 807.
- [11] S. A. U. Hasan, Y. Jung, S. Kim, C. L. Jung, S. Oh, J. Kim, H. Lim, *Sensors* **2016**, *16*, 93.
- [12] X. Li, W. Huang, G. Yao, M. Gao, X. B. Wei, Z. W. Liu, H. Zhang, T. X. Gong, B. Yu, *Scr. Mater.* **2017**, *129*, 61.
- [13] B. Liang, W. Chen, Z. He, R. Yang, Z. Lin, H. Du, Y. Shang, A. Cao, Z. Tang, X. Gui, *Small* **2017**, *13*, 1702422.
- [14] L. Pan, A. Chortos, G. Yu, Y. Wang, S. Isaacson, R. Allen, Y. Shi, R. Dauskardt, Z. Bao, *Nat. Commun.* **2014**, *5*, 3002.
- [15] H. Park, Y. R. Jeong, J. Yun, S. Y. Hong, S. Jin, S. J. Lee, G. Zi, J. S. Ha, *ACS Nano* **2015**, *9*, 9974.
- [16] T. Yang, W. Wang, H. Zhang, X. Li, J. Shi, Y. He, Q. S. Zheng, Z. Li, H. Zhu, *ACS Nano* **2015**, *9*, 10867.
- [17] Y. Zhu, J. Li, H. Cai, Y. Wu, H. Ding, N. Pan, X. Wang, *Sens. Actuators, B* **2018**, *255*, 1262.
- [18] C. Rendl, P. Greindl, M. Haller, M. Zirkl, B. Stadlober, P. Hartmann, *UIST'12*, ACM, Cambridge, MA, USA **2012**, p. 509.
- [19] J. Engel, J. Chen, N. Chen, S. Pandya, C. Liu, presented at *IEEE MEMS*, Istanbul, Turkey, January **2006**.
- [20] H. K. Kim, S. Lee, K. S. Yun, *Sens. Actuators, A* **2011**, *165*, 2.
- [21] H. Kou, L. Zhang, Q. Tan, G. Liu, W. Lv, F. Lu, H. Dong, J. Xiong, *Sens. Actuators, A* **2018**, *277*, 150.
- [22] B. Y. Lee, J. Kim, H. Kim, C. Kim, S. D. Lee, *Sens. Actuators, A* **2016**, *240*, 103.
- [23] H. K. Lee, S. I. Chang, E. Yoon, *J. Microelectromech. Syst.* **2006**, *15*, 1681.
- [24] D. J. Lipomi, M. Vosgueritchian, B. C. Tee, S. L. Hellstrom, J. A. Lee, C. H. Fox, Z. Bao, *Nat. Nanotechnol.* **2011**, *6*, 788.
- [25] S. C. Mannsfeld, B. C. Tee, R. M. Stoltenberg, C. V. Chen, S. Barman, B. V. Muir, A. N. Sokolov, C. Reese, Z. Bao, *Nat. Mater.* **2010**, *9*, 859.
- [26] B. Nie, R. Li, J. Cao, J. D. Brandt, T. Pan, *Adv. Mater.* **2015**, *27*, 6055.
- [27] Y. Quan, X. Wei, L. Xiao, T. Wu, H. Pang, T. Liu, W. Huang, S. Wu, S. Li, Z. Chen, *J. Alloys Compd.* **2017**, *699*, 824.
- [28] J. I. Yoon, K. S. Choi, S. P. Chang, *Microelectron. Eng.* **2017**, *179*, 60.
- [29] G. Schwartz, B. C. Tee, J. Mei, A. L. Appleton, D. H. Kim, H. Wang, Z. Bao, *Nat. Commun.* **2013**, *4*, 1859.
- [30] H. B. Palmer, *Electrical Eng.* **1937**, *56*, 363.
- [31] S.-C. Wong, P. S. Liu, J.-W. Ru, S.-T. Lin, *Solid-State Electron.* **1998**, *42*, 969.
- [32] Y. W. Choi, D. Kang, P. V. Pikhitsa, T. Lee, S. M. Kim, G. Lee, D. Tahk, M. Choi, *Sci. Rep.* **2017**, *7*, 40116.
- [33] G. Y. Bae, S. W. Pak, D. Kim, G. Lee, D. H. Kim, Y. Chung, K. Cho, *Adv. Mater.* **2016**, *28*, 5300.
- [34] J. Park, Y. Lee, J. Hong, M. Ha, Y.-D. Jung, H. Lim, S. Y. Kim, H. Ko, *ACS Nano* **2014**, *8*, 4689.
- [35] J. Park, M. Kim, Y. Lee, H. S. Lee, H. Ko, *Sci. Adv.* **2015**, *1*, e1500661.
- [36] L. Cai, S. Zhang, Y. Zhang, J. Li, J. Miao, Q. Wang, Z. Yu, C. Wang, *Adv. Mater. Technol.* **2018**, *3*, 1700232.
- [37] D. J. Lipomi, J. A. Lee, M. Vosgueritchian, B. C.-K. Tee, J. A. Bolander, Z. Bao, *Chem. Mater.* **2012**, *24*, 373.
- [38] Y. Wang, C. Zhu, R. Pfattner, H. Yan, L. Jin, S. Chen, F. Molina-Lopez, F. Lissel, J. Liu, N. I. Rabiah, Z. Chen, J. W. Chung, C. Linder, M. F. Toney, B. Murmann, Z. Bao, *Sci. Adv.* **2017**, *3*, e1602076.
- [39] H. Shi, T. Pinto, Y. Zhang, C. Wang, X. Tan, *Proc. SPIE 10597, Nano-, Bio-, Info-Tech Sensors, and 3D Systems II*, SPIE, Denver, CO, USA **2018**.
- [40] ASTM International, ASTM D412-15a, <https://doi.org/10.1520/D0412-15A> (accessed: December 2015).
- [41] M. Mooney, *J. Appl. Phys.* **1940**, *11*, 582.
- [42] R. S. Rivlin, *Philos. Trans. R. Soc., A* **1948**, *241*, 379.
- [43] O. H. Yeoh, *Rubber Chem. Technol.* **1993**, *66*, 754.
- [44] R. W. Ogden, *Proc. R. Soc. A* **1972**, *326*, 1567.